Electronic Supplementary Material (ESI) for Inorganic Chemistry Frontiers.

Iron Covalent Doping in WB_2 to Boost Hydrogen Evolution Activity

Meng Jin,[a,b,‡] *Yanyan Liu,*[a,b,‡] *Jialu Wang,*[a,b] *Xian Zhang,*[*a,b] *Miaomiao Han,*[*c] *Yunxia Zhang,*[a,b] *Guozhong Wang,*[a,b] *Haimin Zhang,*[*a,b]

[a] Key Laboratory of Materials Physics, Centre for Environmental and Energy Nanomaterials, Anhui Key Laboratory of Nanomaterials and Nanotechnology, CAS Center for Excellence in Nanoscience Institute of Solid State Physics, HFIPS, Chinese Academy of Sciences, Hefei 230031, (P.R. China)

[b] University of Science and Technology of China, Hefei 230026, (P.R. China)

[c] School of Science, Huzhou University, Huzhou, Zhejiang 313000, (P.R. China)

[‡] These authors contributed equally to this work.

[*] Corresponding author: E-mail: zhangxian158229@163.com, mmhan@zjhu.edu.cn, zhanghm@issp.ac.cn.

Experimental Section

Chemicals and Materials

All the used chemicals were analytical pure without additional purification. Amorphous boron powder (B), ferric trichloride ($FeCl_3$), potassium chloride (KCl), and sodium chloride (NaCl), sodium hydroxide (NaOH) were purchased from Sinopharm Chemical Reagent Co. Ltd. Tungsten pentachloride (WCl_5), ethanol (C_2H_5OH) were purchased from Aladdin reagent Co. Ltd.

Sample preparation

In a typical synthetic process, the tungsten diborides were prepared by boron thermal reduction in molten salts similar to previous reports.[1] In detail, 0.595 g of WCl_5, 0.1 g $FeCl_3$ and 0.13 g of boron powder were added 5.0 g of NaCl-KCl-KOH mixture with the NaCl: KCl: NaOH ratio of 1:1:0.05. Then, the mixture powder above is thoroughly ground in a mortar for 1 hour. The mixture was placed into an Al_2O_3 crucible and then heated at 1000 ^oC for 1 h in a tubular furnace under Ar atmosphere, the heating rate was 10 ^oC min^{-1}. After cooling, a block of salt in the crucible was washed three times with warm water of 80 ^oC to remove the inorganic salts and the by-products B_yO_z. The final sample was washed with ethanol and dried in a vacuum drying oven at 80 ^oC. Similar to Fe covalent-doped WB_2, the pure WB_2 was prepared without the addition of $FeCl_3$.

Preparation of WB_2 and Fe-WB_2 Electrode

The catalyst ink was prepared by dissolving 10 mg catalyst powder with 20 μL Nafion D520, 20 μL deionized water, and 960 μL ethanol in an ultrasonic bath for 30

min. Then 100 μL catalyst ink was coated on a 1.0×1.0 cm^2 of carbon cloth and dried under room temperature.

Materials Characterizations

The crystalline structures of pure WB_2 and Fe covalent-doped WB_2 samples were identified by powder X-ray diffraction analysis (XRD, Philips X'pert PRO) using Nifiltered monochromatic CuKa radiation ($\lambda_{K\alpha1}$=1.5418 Å) at 40 kV and 40 mA. The samples microstructure was further studied through field emission scanning electron microscopy (FESEM, Quanta 200FEG) and transmission electron microscopy (TEM, JEOL 2010) with an energy dispersive X-ray spectrometer (EDS Oxford, Link ISIS). X-ray photoelectron spectroscopy (XPS) analysis was performed on an ESCALAB 250 X-ray photoelectron spectrometer (Thermo, America) equipped with Al Kα1,2 monochromatized radiation at 1486.6 eV X-ray source.

Electrochemical measurements

The electrochemical measurements were conducted on a CHI 760E electrochemical workstation purchased from CH Instruments, Inc. in a three-electrode system. A saturated Ag/AgCl electrode was used as the reference electrode, a Pt mesh was used as the counter electrode and the catalysts were coated on carbon cloth as the working electrode. To activate the electrochemical surface, several repeated cyclic voltammetry was performed. And the as-prepared electrodes were tested in 0.5 M H_2SO_4 or 0.05 M H_2SO_4 solution after activation. The polarization curves were obtained from the linear sweep voltammetry (LSV) with a scan rate of 10 mV s^{-1}. Electrochemical impedance spectroscopy (EIS) results were tested in the frequency

range of 0.1-1000 Hz at corresponding conditions. All potentials are calibrated to the reversible hydrogen electrode (RHE) according to the following equation (1):

$$E_{RHE} = E_{Ag/AgCl} + 0.059pH + E^{0}_{Ag/AgCl} \quad (1)$$

where E_{RHE} is the converted potential (V) vs. RHE, $E^{o}_{Ag/AgCl} = 0.197$ V at 25 °C, and $E_{Ag/AgCl}$ is the experimentally measured potential against Ag/AgCl reference electrode.

Determination of ammonia

The indophenol blue method[2] was adopted for the detection of the produced ammonia. Specifically, a certain electrolyte after catalysis was taken out from the cathode compartment and was first diluted with deionized water in order to ensure the ammonia concentrations were in the linear range of the indophenol blue method. Next, 500 μL of 1.0 m NaOH solution containing sodium citrate (5.0 wt%) and salicylic (5.0 wt%) was added to the abovementioned solution. Then, the color agent composed of 100 μL of sodium nitroferricyanide solution (1.0 wt%) and 100 μL of NaClO solution (0.55 m) was added to the abovementioned solution. The mixture was detected via the ultraviolet-visible (UV-vis) spectrophotometer. After sitting for 1 hour, the absorbance at the wavelength of 697 nm was recorded.

Determination of hydrazine (N_2H_4)

The Watt and Chrisp method[3] was adopted for the detection of N_2H_4. Firstly, a certain electrolyte after catalysis was taken out from the cathode compartment and was acidized with 1.0 M HCl solution. Subsequently, the 5.0 mL color reagent containing p-C9H11NO (5.99 g), HCl (30 mL), and C_2H_5OH (300 mL) was added to the

abovementioned solution. After standing at room temperature for 20 min, the absorbance intensity was measured at a wavelength of 455 nm.

Calculation of NH_3 Yield and Faradaic efficiency (FE)

$$FE=(3\times F\times C\times V)/Q\times 100\%$$

$$NH_3\ Yield=(14\times C\times V)/(t\times S)$$

where the Faradaic constant (96485 C mol^{-1}), C is the mass concentration of NH_4^+－N, V is the volume of electrolyte, Q is the total charge.14 is the N atom molar mass, t is the reaction time, S is the geometric area of working electrode.

Isotope Labeling Experiments

The isotope labeling experiments were conducted using $^{14}N_2$ and $^{15}N_2$ as the feeding gases (99% enrichment of ^{15}N in $^{15}N_2$, supplied by Hefei Ninte Gas Management Co., Ltd.) To eliminate the possible pollutants (such as NO_x and NH_3), the feeding gases were first passed through the 1.0×10^{-3} M H_2SO_4 solution and water.[4] After NRR reaction, the obtained $^{15}NH_3$ mixed with 0.1 mL D_2O was detected by the ^1H NMR spectroscopy measurement (Bruker AVANCE AV III 600).

Computational Details ：

All the spin-polarized DFT calculations were performed using the Vienna Ab-initio Simulation Package (VASP),[5] and the generalized gradient approximation (GGA) with the Perdew-Burke-Ernzerhof (PBE) exchange-correlation functional was used with the projector augmented wave method.[6] A kinetic energy cutoff of 400 eV was used for plane wave expansion, the convergence threshold was set as 10^{-5} eV in energy and 0.02 eV $Å^{-1}$ in force. The Brillouin zone was sampled with a 9 × 9 × 3, 5 ×

5 × 1 and 5 × 5 × 1 Monkhorst-Pack k-points grid for geometric optimization of bulk WB_2, pure WB_2, and Fe-WB_2 slab models, respectively. The vacuum distance was set to 15 Å to minimize the artificial interactions of the interlayer.[7] During the total calculations, the symmetry was switched off and the dipolar correction was also included. DFT-D3 method was used for the dispersion correction.[8] Here, the elementary steps can be summarized as follows:

$$* + N_2 \rightarrow *N_2$$

$$*N_2 + H^+ + e^- \rightarrow *NNH$$

$$*NNH + H^+ + e^- \rightarrow *NHNH$$

$$*NNH + H^+ + e^- \rightarrow *NNH_2$$

$$*NNH_2 + H^+ + e^- \rightarrow NH_3 + *N$$

$$N* + H^+ + e^- \rightarrow *NH$$

$$*NH + H^+ + e^- \rightarrow *NH_2$$

$$*NH_2 + H^+ + e^- \rightarrow NH_3 + *$$

Then, the Gibbs free energy of the NRR reaction pathways was referenced to the computational hydrogen electrode (CHE) model, which proposed by Nørskov and co-workers.[7]

$$\triangle G = \triangle E + \triangle ZPE - T\triangle S$$

where $\triangle E$ is electronic energy difference, $\triangle ZPE$ is the difference of zero-point energy, T is the temperature (T = 298.15 K), and ΔS is the entropy change.

The results of the crystal orbital Hamiltonian population (COHP) analysis was obtained by LOBSTER code.[9-12] And the VASPKIT code was used for the post-processing of VASP calculation data.[13]

Table S1. *N_2 vertical adsorption energy at different terminals of pure WB_2 and Fe-WB_2.

Termination type	Adsorption sites	Adsorption energy
Fe-WB_2	Fe-terminated slab	−0.769
Fe-WB_2	W1-terminated slab	−1.432
Fe-WB_2	W2-terminated slab	−1.194
Fe-WB_2	B1-terminated slab	unstable
Fe-WB_2	B2-terminated slab	unstable
WB_2	W1-terminated slab	−1.336
WB_2	W2-terminated slab	−1.019
WB_2	B1-terminated slab	0.654
WB_2	B2-terminated slab	−1.106

Table S2. Electrocatalytic hydrogenation of nitrogen in the reported literature.

Electrocatalyst	Conditions	NH_3 Production Rate	Faradaic Efficiency (%)	Reference
BCN	0.1 M HCl	7.75 μg h^{-1} mg_{cat}^{-1} (−0.3 V *vs.* RHE)	13.79	14
B/N–CNF	0.1 M KOH	32.5 μg h^{-1} mg_{cat}^{-1} (−0.5 V *vs.* RHE)	13.2	15
B-doped TiO_2	0.1 M Na_2SO_4	14.4μg h^{-1} mg_{cat}^{-1} (−0.8 V *vs.* RHE)	3.4	16
B-doped Bi nanorolls	0.05 M Na_2SO_4	29.2 mg_{NH3} g_{cat}^{-1} h^{-1} (0.48 V *vs.* RHE)	8.3	17
BNS	0.1 M Na_2SO_4	13.22 mg_{NH3} g_{cat}^{-1} h^{-1} (-0.8 V *vs.* RHE)	4.04	18
BNC-NSs	0.05 M Na_2SO_4	15.7 μg h^{-1} mg_{cat}^{-1} (−0.4 V *vs.* RHE)	8.10	19
BP/CP	0.1 M HCl	26.42 μg h^{-1} mg_{cat}^{-1} (-0.6 V *vs.* RHE)	12.7	20
B–Ag NSs	0.1 M HCl	26.48 μg h^{-1} mg_{cat}^{-1} (-0.5 V *vs.* RHE)	8.86	21

np-B	0.05 M Na_2SO_4	23.11 μg h^{-1} mg_{cat}^{-1} (-0.4 V *vs.* RHE)	25.17	22
B, O-CMS	0.1 M HCl	19.2μg h^{-1} mg_{cat}^{-1} (-0.25 V *vs.* RHE)	5.57	23

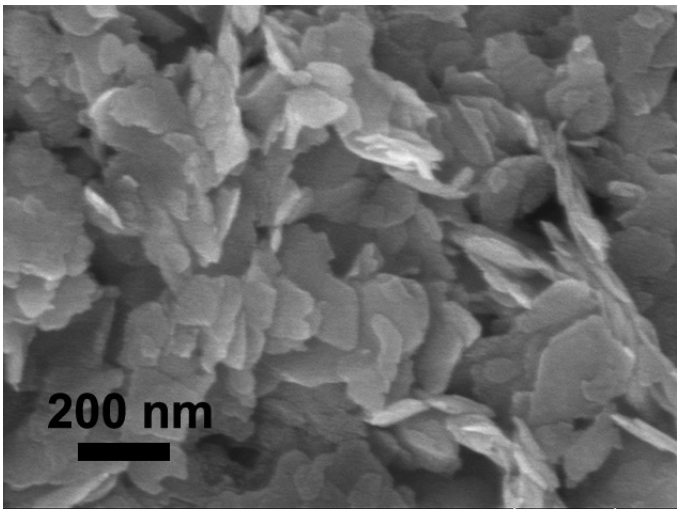

Figure S1. The SEM image of pristine WB_2.

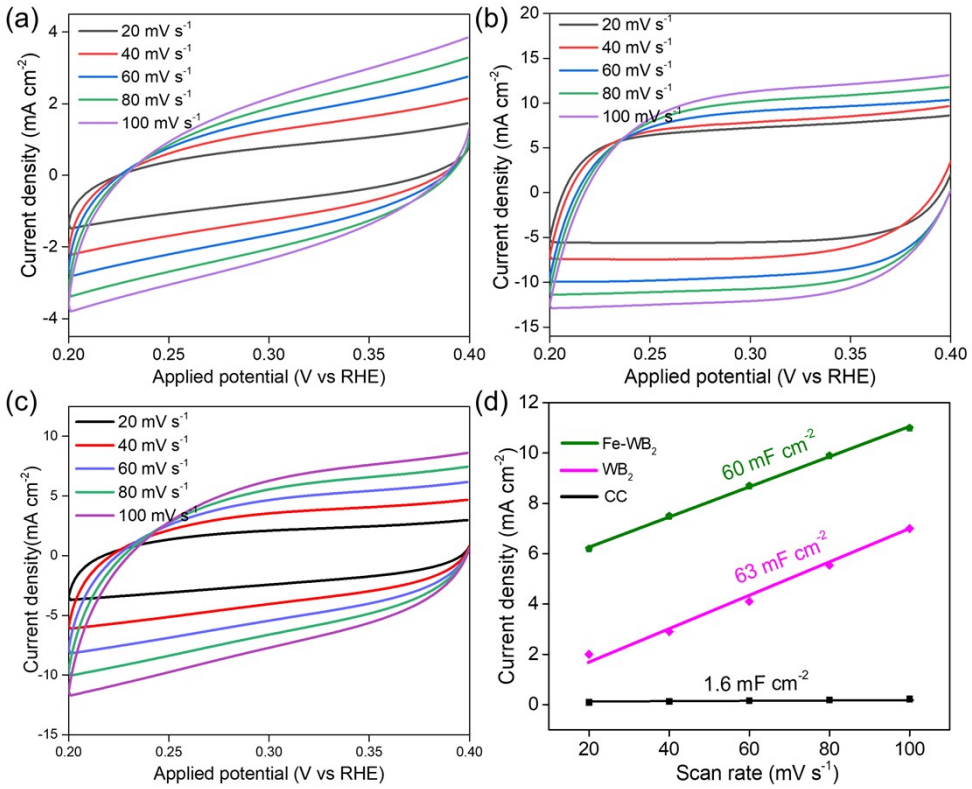

Figure S2. The double-layer capacitance for (a) CC (b) Fe-WB_2 (c) WB_2 determines

the slope of the line.

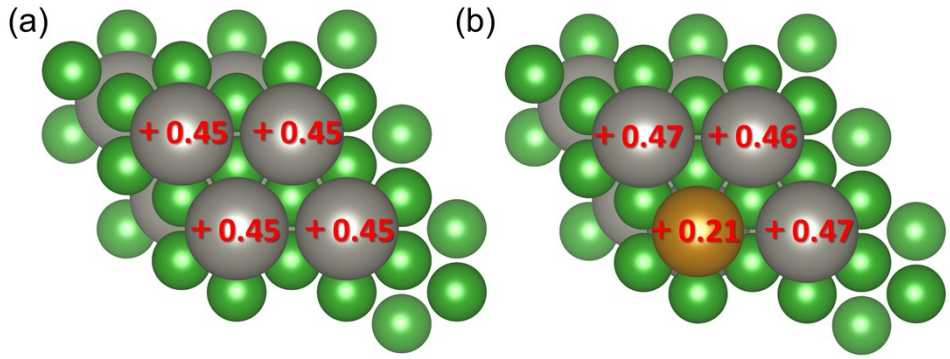

Figure S3. Bader charge analysis of (a) WB_2(001) (b) Fe-WB_2(001). Color code: green, B; dark gray, W; yellow, Fe; blue, N; pink, H. (The positive and negative value means lose electrons and get electrons)

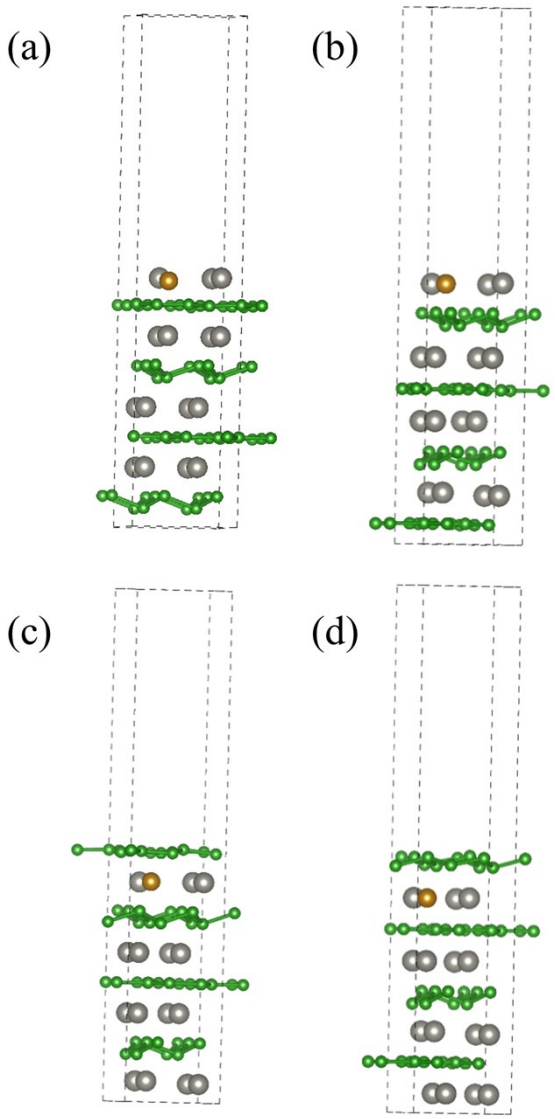

Figure S4. (a-d) The Fe-WB_2 (001) four different terminated slabs. Four terminated slabs were represented as follows. (a) W1-terminated and Fe-terminated represents the metal directly connected to graphene-like boron layer, (b) W2-terminated represents the metal directly connected to cyclohexane-like chair boron. (c) B1-terminated represents the graphene-like boron layer and (d) B2-terminated represents the cyclohexane-like chair boron layer. Color code: green, B; gray, W; yellow, Fe.

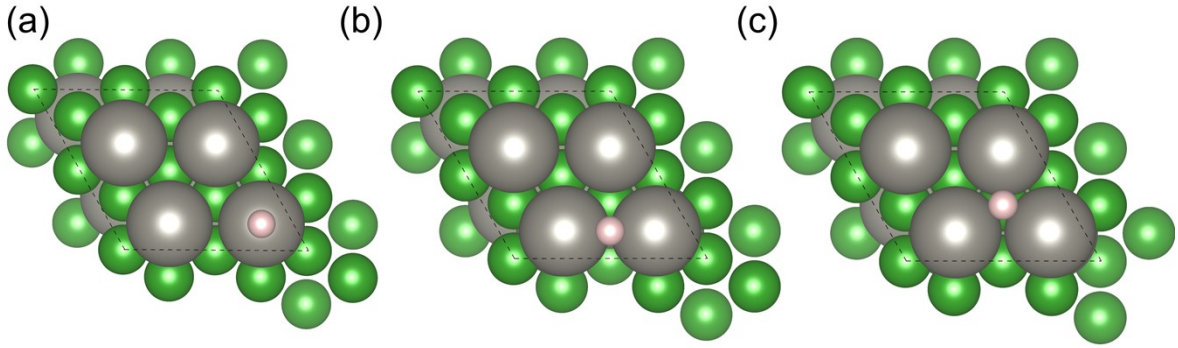

Figure S5. Different stable H* adsorption sites of pure WB_2 (001) (a) top (b) bridge (c) hollow site. Color code: green, B; dark gray, W; yellow, Fe; pink, H.

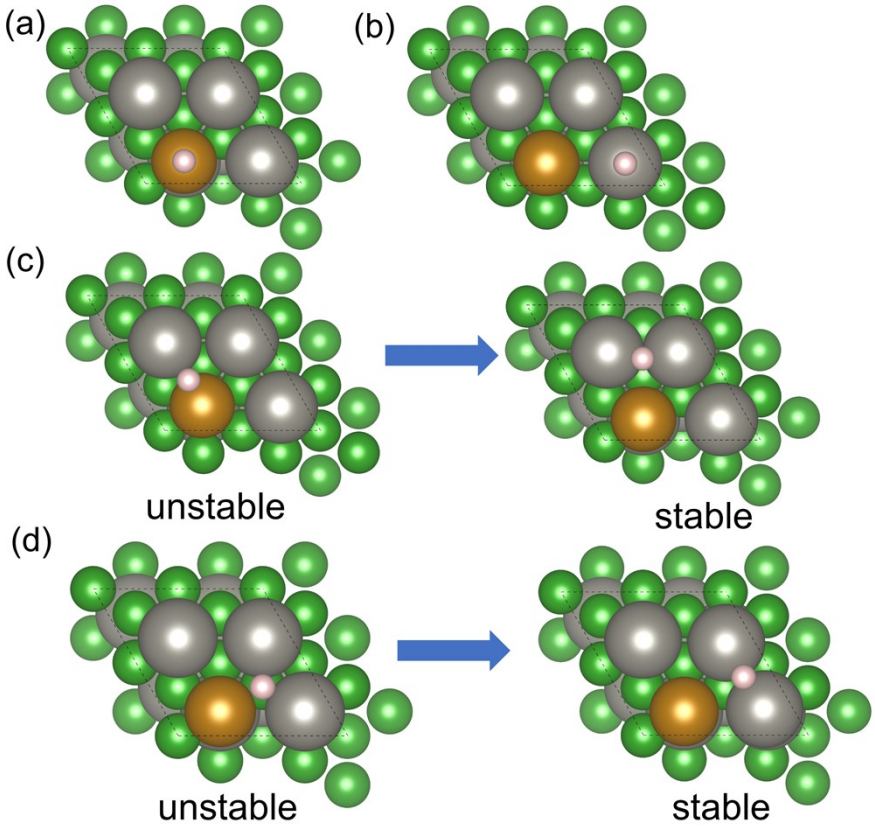

Figure S6. Different stable H* adsorption sites of Fe-WB_2 (001) (a) top site on Fe atom (b) top site on W site (c) bridge site (H is unstable in the Fe-W bridge position and will be optimized to the W-W bridge position) (d) hollow site (H is unstable in

the hollow position and will be optimized to the bridge position). Color code: green, B; dark gray, W; yellow, Fe; blue, N; pink, H.

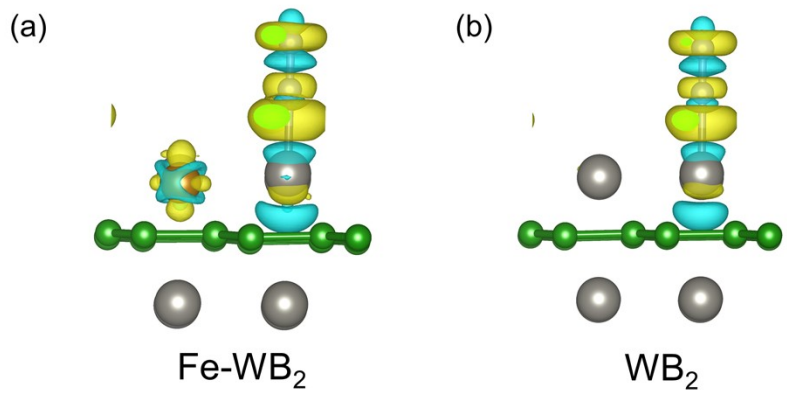

Figure S7. Deformation charge density of (a) Fe-WB_2 and (b) WB_2. Isosurface=0.0021 eA^{-3}. Yellow and cyan represent electron accumulation and depletion. Color code: green, B; gray, W; yellow, Fe； blue, N.

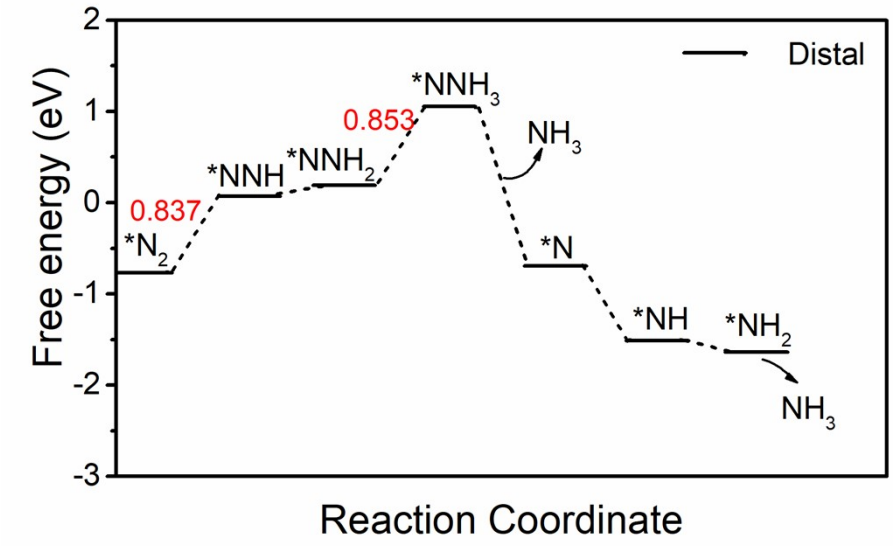

Figure S8. Free energy diagrams for NRR on pure WB_2(001).

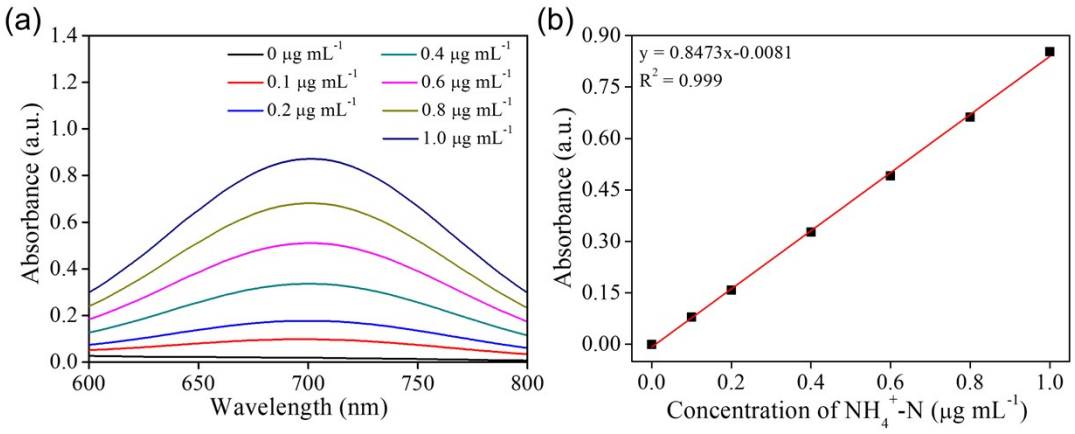

Figure S9. a) UV-Vis absorbance spectra of the indophenol blue indicator with different concentrations of NH_4^+ ions after incubating for 1 h at room temperature. b) Calibration curve obtained from the absorbance at a wavelength of 697 nm as a function of the various NH_4Cl concentrations

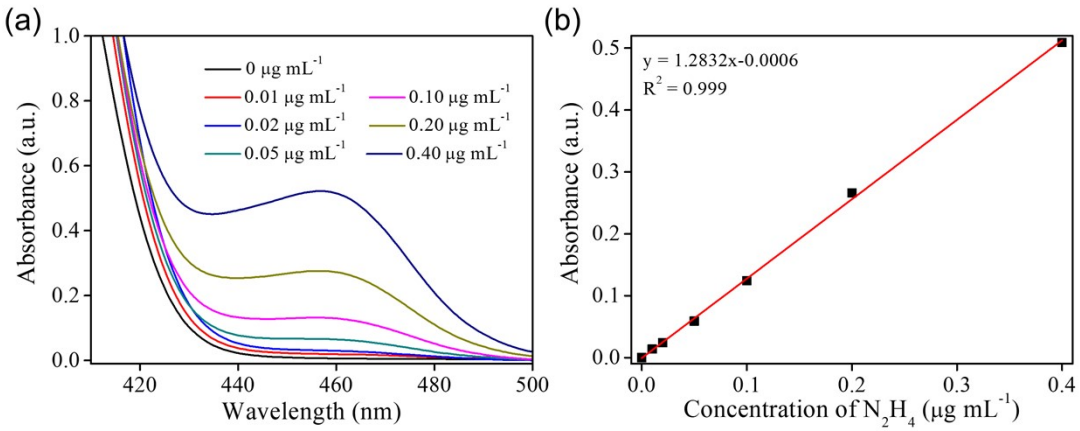

Figure S10. (a) UV-Vis absorbance spectra of different concentrations of $N_2H_4 \cdot H_2O$ with the Watt and Chrisp method (b) Calibration curve of absorbance vs various concentrations of N_2H_4.

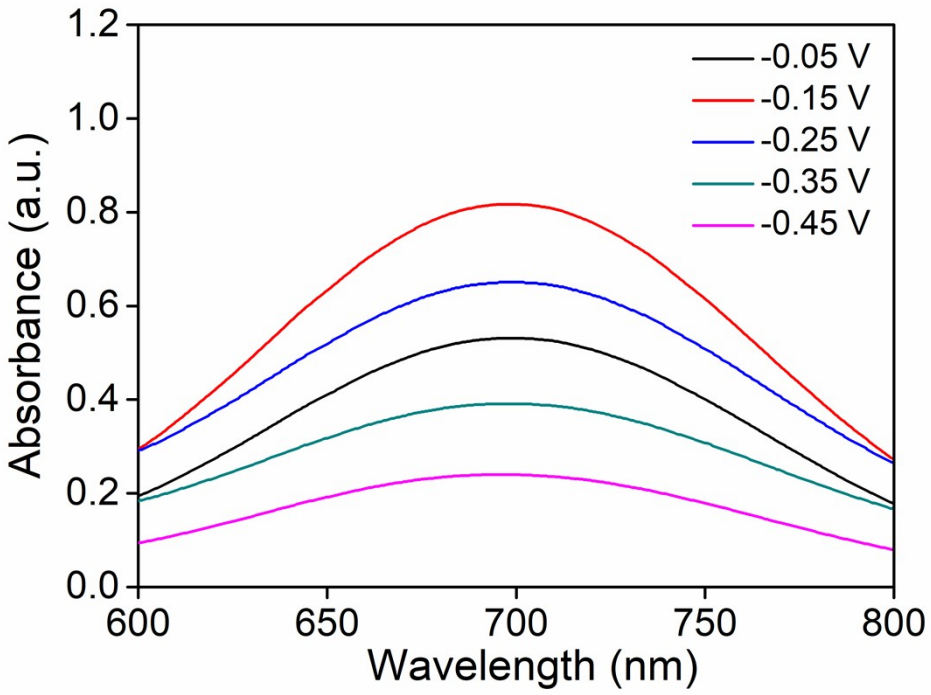

Figure S11. UV-visible colorimetric spectra on Fe-WB_2 at different voltages.

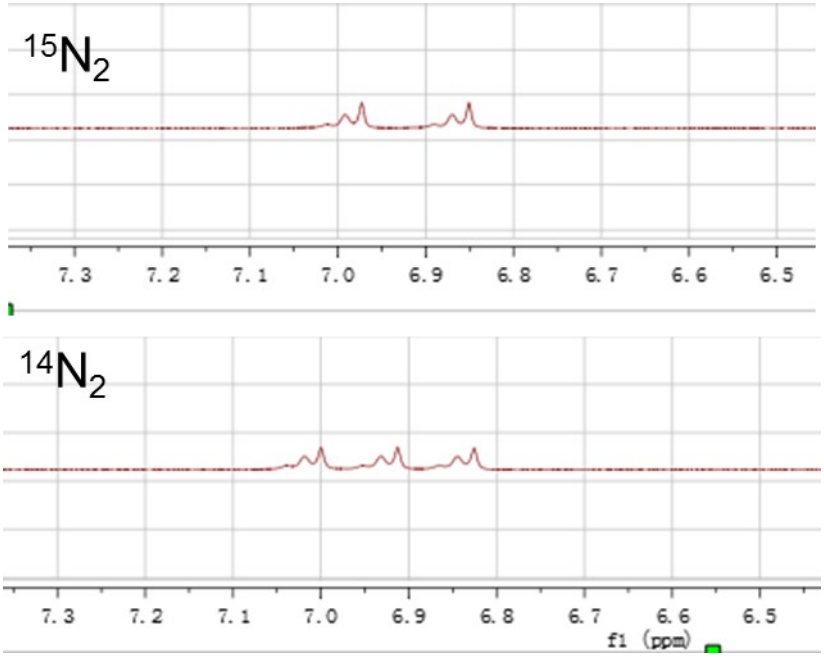

Figure S12. The presence of $^{14}NH_4^+$ and $^{15}NH_4^+$ can quantify the NH_3 generation using ^{1}HNMR.

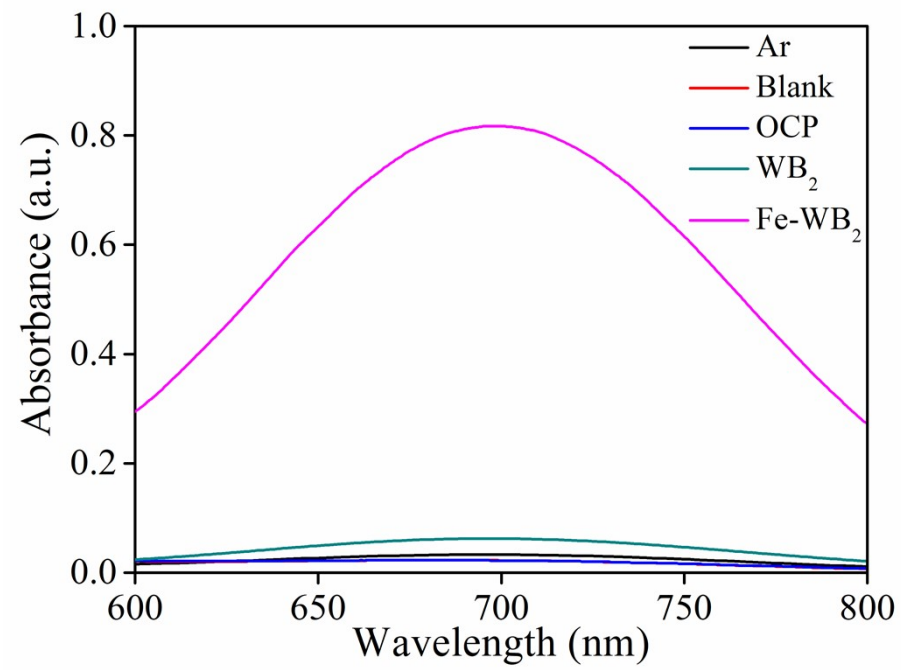

Figure S13. UV-vis absorbance spectra for the NRR on different reaction conditions.

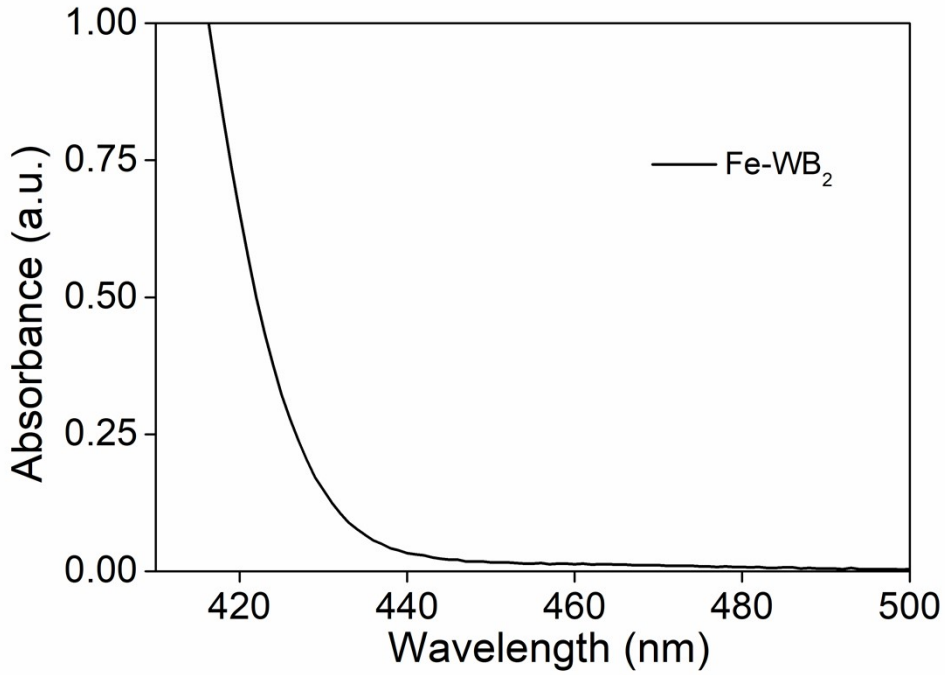

Figure S14. UV-vis absorbance spectra of the anode compartment after potentiostatic tests for the NRR on Fe-WB_2 electrode.

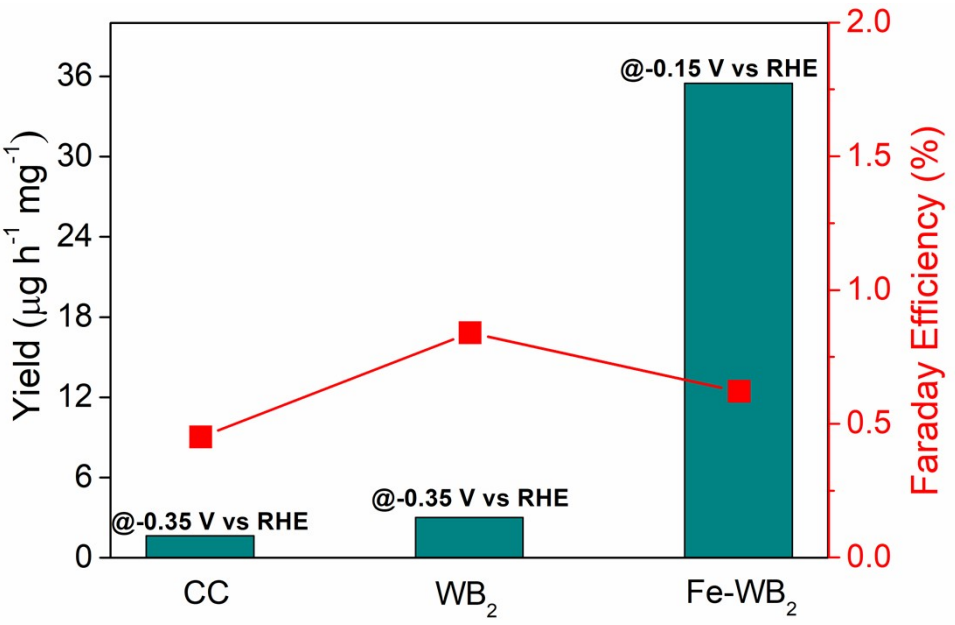

Figure S15. The maximum of the NH_3 yields and FE for CC, WB_2 and Fe-WB_2 catalysts.

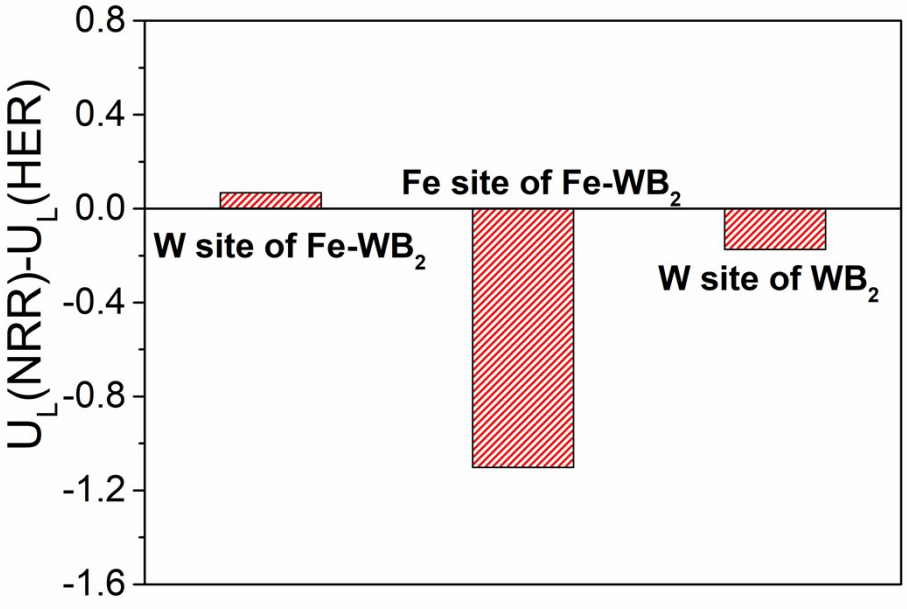

Figure S16. Difference between the limiting potential of NRR and HER

References

1. Q. Li, L. Wang, X. Ai, H. Chen, J. Zou, G.D. Li, X. Zou, Multiple crystal phases of intermetallic tungsten borides and phase-dependent electrocatalytic property for hydrogen evolution, Chem. Commun., 2020, **56**, 13983-13986.

2. D. Zhu, L. Zhang, R.E. Ruther, R.J. Hamers, Photo-illuminated diamond as a solid-state source of solvated electrons in water for nitrogen reduction, Nat. Mater., 2013, **12**, 836-841.

3. G.W. Watt, J.D. Chrisp, Spectrophotometric method for determination of hydrazine, Anal. Chem., 1952, **24**, 2006-2008.

4. F. Zhou, L.M. Azofra, M. Ali, M. Kar, A.N. Simonov, C. McDonnell-Worth, C. Sun, X. Zhang, D.R. MacFarlane, Electro-synthesis of ammonia from nitrogen at ambient temperature and pressure in ionic liquids, Energy Environ. Sci., 2017, **10**, 2516-2520.

5. G. Kresse, J. Hafner, Ab initio molecular-dynamics simulation of the liquid-metal--amorphous-semiconductor transition in germanium, Phys. Rev. B, 1994, **49**, 14251-14269.

6. J.P. Perdew, K. Burke, M. Ernzerhof, Generalized gradient approximation made simple, Phys. Rev. Lett., 1996, **77**, 3865-3868.

7. J.K. Nørskov, J. Rossmeisl, A. Logadottir, L. Lindqvist, J.R. Kitchin, T. Bligaard, H. Jónsson, Origin of the overpotential for oxygen reduction at a fuel-cell cathode, J. Phys. Chem. B, 2004, **108**, 17886-17892.

8. S. Grimme, Semiempirical GGA-type density functional constructed with a long-range dispersion correction, J. Comput. Chem., 2006, **27**, 1787-1799.

9. S. Maintz, V.L. Deringer, A.L. Tchougréeff, R. Dronskowski, Analytic projection from plane-wave and PAW wavefunctions and application to chemical-bonding analysis in solids, J. Comput. Chem., 2013, **34**, 2557-2567.

10. V.L. Deringer, A.L. Tchougréeff, R. Dronskowski, Crystal Orbital Hamilton Population (COHP) Analysis As projected from plane-wave basis sets, J. Phys. Chem. A, 2011, **115**, 5461-5466.

11. R. Dronskowski, P.E. Bloechl, Crystal orbital Hamilton populations (COHP):

energy-resolved visualization of chemical bonding in solids based on density-functional calculations, J. Phys. Chem., 1993, **97**, 8617-8624.

12. S. Maintz, V.L. Deringer, A.L. Tchougréeff, R. Dronskowski, LOBSTER: A tool to extract chemical bonding from plane-wave based DFT, J. Comput. Chem., 2016, 37, 1030-1035.

13. V. Wang, N. Xu, J.-C. Liu, G. Tang, W.T. Geng, VASPKIT: A user-friendly interface facilitating high-throughput computing and analysis using VASP code, Comput. Phys. Commun., 2021, **267**, 108033.

14. C. Chen, D. Yan, Y. Wang, Y. Zhou, Y. Zou, Y. Li, S. Wang, B-N Pairs enriched defective carbon nanosheets for ammonia synthesis with high efficiency, Small, 2019, 15, 1805029.

15. Y. Kong, Y. Li, B. Yang, Z. Li, Y. Yao, J. Lu, L. Lei, Z. Wen, M. Shao, Y. Hou, Boron and nitrogen co-doped porous carbon nanofibers as metal-free electrocatalysts for highly efficient ammonia electrosynthesis, J. Mater. Chem. A, 2019, **7**, 26272-26278.

16. Y. Wang, K. Jia, Q. Pan, Y. Xu, Q. Liu, G. Cui, X. Guo, X. Sun, Boron-doped TiO_2 for efficient electrocatalytic N_2 fixation to NH_3 at ambient conditions, ACS Sustain. Chemi. Eng., 2019, **7**, 117-122.

17. F. Xu, F. Wu, K. Zhu, Z. Fang, D. Jia, Y. Wang, G. Jia, J. Low, W. Ye, Z. Sun, P. Gao, Y. Xiong, Boron doping and high curvature in Bi nanorolls for promoting photoelectrochemical nitrogen fixation, Appl. Catal. B: Environ., 2021, **284**, 119689.

18. X. Zhang, T. Wu, H. Wang, R. Zhao, H. Chen, T. Wang, P. Wei, Y. Luo, Y. Zhang, X. Sun, Boron nanosheet: an elemental two-dimensional (2D) material for ambient electrocatalytic N_2-to-NH_3 fixation in neutral media, ACS Catal., 2019, **9**, 4609-4615.

19. S. Xiao, F. Luo, H. Hu, Z. Yang, Boron and nitrogen dual-doped carbon nanospheres for efficient electrochemical reduction of N_2 to NH_3, Chem. C0mmun., 2020, **56**, 446-449.

20. X. Zhu, T. Wu, L. Ji, C. Li, T. Wang, S. Wen, S. Gao, X. Shi, Y. Luo, Q. Peng, X. Sun, Ambient electrohydrogenation of N_2 for NH_3 synthesis on non-metal boron phosphide nanoparticles: the critical role of P in boosting the catalytic activity, J. Mater. Chem. A, 2019, **7**, 16117-16121.

21. Y. Li, H. Yu, Z. Wang, S. Liu, Y. Xu, X. Li, L. Wang, H. Wang, Boron-doped silver nanosponges with enhanced performance towards electrocatalytic nitrogen reduction to ammonia, Chem. Commun., 2019, **55**, 14745-14748.

22. J. Lan, M. Peng, P. Liu, D. Chen, X. Xu, M. Luo, Y. Tan, M. Chen, Scalable synthesis of nanoporous boron for high efficiency ammonia electrosynthesis, Mater. Today, 2020, **38**, 58-66.

23. M. Tang, X. Jiang, M. He, N. Jiang, Q. Zheng, D. Lin, B (boron), O (oxygen) dual-doped carbon spheres as a high-efficiency electrocatalyst for nitrogen reduction, Int. J. Hydrog. Energy, 2021, **46**, 439-448.